# TUNABLE LIQUID LENS COMPENSATION OF FIELD CURVATURE IN MEMS-BASED MINIATURIZED MICROSCOPES FOR OPTOGENETIC APPLICATIONS

*Jintao Zhang[1, 2], Yongyu Zhang[2]*
*[1]Ningxia Xiangrui Intelligent Technology Co. Ltd; Yinchuan 750001, China*
*[2]Guangdong Shenliannao Technology Co. Ltd; Foshan 528000, China*

**Abstract** - This paper presents a design and optical simulation study of field curvature compensation in MEMS-based miniaturized microscopes for optogenetic applications. In dual-path systems combining single-photon calcium imaging with targeted optogenetic stimulation, MEMS mirror deflection introduces field curvature aberration that causes the stimulation laser focal point to shift axially away from the imaging plane, severely compromising single-cell targeting accuracy. We analyze this problem using Petzval sum theory and propose dynamic compensation via an electrically-tunable liquid lens placed in the stimulation optical path. Through TracePro optical simulation, we characterize the axial focal shift at deflection angles up to 3.8° (maximum 0.82 mm along the X-axis, 0.22 mm along the Y-axis) and determine the liquid lens curvature required to compensate field curvature across all scanning directions, including the X-axis, Y-axis, and two diagonal directions. The compensation relationship is established by polynomial fitting of 21 simulated data points per axis and extended to full two-dimensional coverage via three-dimensional polynomial surface fitting in MATLAB. With the optimal 4th-order polynomial model ($R^2 = 0.9982$), the compensation method achieves a 7-fold improvement in mean axial positioning accuracy (from 42.3 μm to 5.8 μm), reducing the maximum error from 73.2 μm to 12.1 μm-sufficient for single-cell resolution optogenetics (neuronal soma diameter 10-20 μm). This work provides a quantitative design framework for field curvature correction in miniaturized MEMS scanning systems, with applications extending to neuroscience, biomedical imaging, and compact scanning devices.

**Keywords**: MEMS; Optogenetics; Field curvature correction; Liquid lens; Miniature microscope; Neural modulation

## 1. Introduction

One of the core objectives of neuroscience research is to understand the activity patterns and functions of neurons and neural circuits during behavior [1, 2]. The emergence of optogenetics has brought revolutionary changes to neuroscience research by enabling millisecond-level temporal precision and cellular-level spatial precision in activating or inhibiting specific neurons through light-sensitive proteins [3, 4]. Combined with calcium imaging technology, researchers can simultaneously record the activity patterns of neuronal populations while modulating neuronal activity, forming a closed-loop experimental paradigm [5, 6].

In recent years, miniaturized head-mounted microscope technology has made significant progress. Miniature single-photon microscopes (miniscopes) and two-photon microscopes can record neuronal activity in freely behaving mice [7-10]. These systems are lightweight (<5 grams) and allow animals to exhibit natural behaviors, greatly expanding the possibilities for neuroscience research. Simultaneously, miniature microscope systems integrating optogenetic stimulation have been rapidly developing, achieving integration of imaging and modulation [11, 12]. However, a critical limitation exists in current miniaturized optogenetic systems: they predominantly employ global or wide-field illumination strategies that lack cellular-level spatial precision. For example, recent work by Stamatakis et al. [11] demonstrated simultaneous optogenetics and calcium imaging using a miniaturized microscope, but the optogenetic stimulation was delivered through wide-field




*dx.doi.org/10.17683/ijomam/issue24.30*

illumination affecting entire brain regions rather than individual neurons. The ability to perform targeted, single-cell-resolution optogenetic stimulation combined with calcium imaging in freely behaving animals remains a significant technical challenge that requires innovative optical design solutions.

Microelectromechanical systems (MEMS) technology offers advantages such as miniaturization, integration, and multifunctionality, and has been widely applied in optical systems [13, 14]. MEMS scanning mirrors can rapidly and precisely control beam direction, demonstrating excellent performance in laser scanning microscopy, optical coherence tomography, and spatial light modulation [15, 16]. In optogenetic applications, MEMS mirrors enable rapid scanning and precise positioning of laser beams, delivering them to specific neuronal locations for cellular-level optogenetic stimulation [17, 18].

However, MEMS mirror deflection introduces a fundamental optical challenge: when the stimulation beam is deflected away from the optical axis, various optical aberrations arise. Among these, field curvature is a major factor causing the stimulation laser focal point to deviate axially from the imaging focal plane [19, 20]. Field curvature causes the natural focal surface to be curved rather than planar, with larger off-axis angles resulting in greater axial displacement of the focal point. In dual-path systems where imaging establishes a planar focal plane and stimulation must target neurons in that plane, this field curvature-induced mismatch severely compromises targeting accuracy. Errors of tens of micrometers can mean stimulating the wrong neurons or missing the intended targets entirely, fundamentally compromising the validity of optogenetic experiments.

Traditional field curvature correction methods include: (1) using combinations of positive and negative lenses to separate optical power; (2) employing high refractive index materials; (3) introducing field lenses; (4) using symmetric or nearly symmetric optical structures; and (5) employing aspheric lenses [21, 22]. However, these methods face significant limitations in miniaturized systems due to constraints on volume, weight, and complexity-critical factors for head-mounted applications in freely behaving animals.

Liquid lenses are tunable optical elements that can adjust focal length and optical power in real-time by controlling the curvature of liquid interfaces through voltage [23-25]. Liquid lenses possess advantages such as fast response speed (millisecond-level), no macroscopic mechanical moving parts, small volume, and low power consumption, and have been applied in adaptive optics, microscopic imaging, and endoscopy [26-28]. Particularly, electrowetting liquid lenses have large focal length adjustment ranges suitable for miniaturized systems [29, 30].

This study addresses the field-curvature problem in MEMS-based scanning systems through optical design and TracePro simulation. We propose an electrically controlled liquid lens in the stimulation path to compensate the Petzval-sum-induced axial shift in real time, using a MEMS-based miniaturized optogenetic microscope that combines single-photon calcium imaging with targeted stimulation as the design context. The results establish a quantitative basis for achieving approximately 10 μm three-dimensional positioning accuracy in a compact head-mounted system, while the broader implications for miniaturized scanning optics are discussed later.

## 2. Methods

### 2.1 System Design

The proposed system employs a dual-path optical design that separates the imaging and optogenetic stimulation functions (Figure 1).

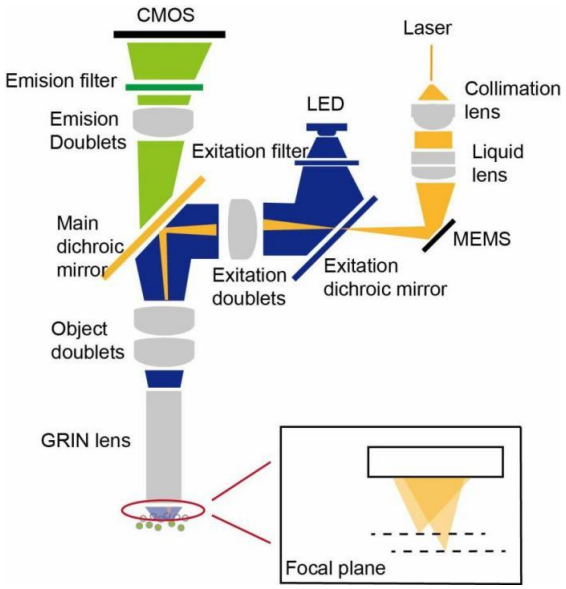


*Figure 1: System optical path schematic showing the dual-path design with imaging path (green) for calcium imaging, calcium excitation path (blue) and optogenetic stimulation path(orange). The MEMS mirror is positioned in the stimulation path, and the liquid lens provides dynamic field curvature compensation*

The imaging path is designed for single-photon calcium imaging of neuronal activity using GCaMP fluorescence (emission: 500-550 nm). This path uses two achromatic doublet lenses (BK7 crown glass + SF5 flint glass) to achieve chromatic aberration correction across the broadband fluorescence spectrum, ensuring high-quality collection of calcium signals.

The imaging path establishes a planar focal plane at the tissue sample where neurons would be visualized. This imaging focal plane remains fixed during operation and defines the reference plane for optogenetic targeting.

The optogenetic stimulation path is designed to deliver 589 nm orange laser light (for ChrimsonR activation) to targeted neurons. This path shares the achromatic doublet lenses with the imaging path but propagates in the opposite direction-the stimulation beam travels backward through the lens system toward the sample. Critically, the stimulation path incorporates a MEMS scanning mirror and an electrically-tunable liquid lens. The MEMS mirror is positioned at the pupil plane and deflects the stimulation beam to different lateral positions (different neurons), while the liquid lens provides dynamic field curvature compensation to maintain axial focus alignment.

The MEMS mirror is positioned at the pupil plane of the system. By adjusting the deflection angles in real-time (X-axis and Y-axis directions), two-dimensional lateral scanning of the stimulation laser beam is achieved across the field of view. The MEMS mirror has an angular resolution of 0.3 degrees, enabling precise control of the lateral position where the stimulation beam is delivered. This allows selective targeting of individual neurons visualized in the calcium imaging.

As the MEMS mirror deflects (moving the stimulation spot laterally), field curvature causes the stimulation focal point to shift axially away from the imaging focal plane. The liquid lens compensates this axial shift by dynamically adjusting its optical power based on the MEMS deflection angle, ensuring the stimulation focus remains aligned with the imaging focal plane at all lateral positions.The key system specifications are summarized in Table 1.

*Table 1. Key specifications of the MEMS-based optogenetic microscope system*

| Serial | Component | Model | Specification | Quantity | Source |
|---|---|---|---|---|---|
| 1 | Collimation lens | #65-568 | 2*9mm FL | 1 | Edmund Optics |
| 2 | Exitation doublets | #63-692 | 4*12mm FL | 1 | Edmund Optics |
| 3 | Object doublets | #45-205 | 4*8mm FL | 2 | Edmund Optics |
| 4 | Emision Doublets | #63-690 | 4*6mm FL | 1 | Edmund Optics |
| 5 | GRIN lens | | 0.5pitch, Φ1.8mm | 1 | |
| 6 | Liquid lens | A-25H0-P07 | | 1 | Corning Incorporated |
| 7 | Exitation filten | ET470 40x | 4*3.5*1mm | 1 | Chroma Optics |
| 8 | Exitation dichroic mirror | T4951pxr | 4*6*1mm | 1 | Chroma Optics |
| 9 | Main dichroic mirror | ZT530/55dcbp-UF1 | 4*6*1mm | 1 | Chroma Optics |
| 10 | Emision filter | ET525/50M | 4*4*1mm | 1 | Chroma Optics |
| 11 | MEMS | A7M10.2-1000AL-LCC20-NC | | 1 | Mirrorcle Technologies |
| 12 | Liquid lens | μTLENSNIR-D-45 | 18 diopters dynamic range | 4 | Polight |

## 2.2 Field Curvature Problem in Optogenetic Stimulation Path

In this dual-path design, the imaging plane defines the planar reference plane at the tissue sample, and the stimulation beam must focus on the same imaged neurons. Any axial deviation between these two planes directly reduces optogenetic targeting precision. When the MEMS mirror directs the stimulation beam to off-axis positions, propagation through the achromatic doublet lenses introduces aberrations.

In this system, field curvature is the dominant source of axial focal error.

According to the Petzval sum, the natural focal surface of the stimulation path is curved rather than planar.

As the MEMS deflection angle increases, the laser focus shifts along the optical axis, creating a depth mismatch relative to the fixed imaging plane.

The Petzval sum quantifies the curvature of this natural focal surface:

$$\frac{1}{r} = \mathrm{P} = \sum \Phi_i / n_i \quad (1)$$

where r is the radius of curvature of the curved surface, P is the Petzval sum, $\varphi_i$ is the optical power of the lens element, and $n_i$ is the refractive index of the lens material.

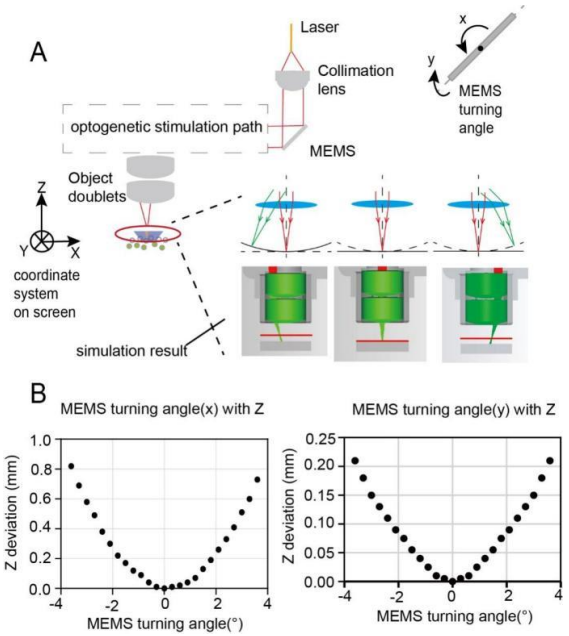


*Figure 2: Schematic illustration of field curvature-induced focal point displacement. (A) Schematic diagram of the axial focal point shift under different MEMS deflection angles: simulation results show that the focal point shifts axially (upward) with increasing MEMS deflection angle. (B) Simulation results of the axial focal shift along the X- and Y-axis deflection directions. The X-direction shift is substantially larger, reaching a maximum of 0.82 mm at a MEMS deflection angle of 3.8°, while the Y-direction shift is smaller, with a maximum of 0.22 mm at 3.8° deflection*

The larger the MEMS deflection angle, the greater the axial displacement of the stimulation focal point from the imaging focal plane (Figure 2). This systematic and predictable deviation has critical implications for neuroscience experiments. When attempting to stimulate a specific neuron visualized in the calcium imaging, the stimulation laser may focus at an incorrect depth-potentially dozens of micrometers away from the intended target neuron. In the design context, understanding and correcting this systematic error is essential for achieving the precision required for cellular-resolution optogenetics.

The axial focal shift varies systematically with lateral position across the field of view. Without correction, stimulation at different lateral positions will have different axial errors, making it impossible to maintain consistent three-dimensional targeting precision across the imaging field. This spatial variability would degrade experimental reproducibility and make it difficult to compare stimulation effects at different locations.

Importantly, this field curvature problem affects only the stimulation path, not the imaging path. The calcium imaging itself remains properly focused at the imaging focal plane. The issue is the mismatch between where neurons would be seen (imaging focal plane) and where the laser would actually focus (displaced stimulation focal point). Therefore, correcting field curvature in the stimulation path is essential for achieving true cellular-resolution optogenetic control in MEMS-based scanning systems.

## 2.3 Field Curvature Compensation Method Using Liquid Lens

The goal of field curvature compensation is to ensure that the stimulation laser focal point always coincides with the imaging focal plane, regardless of MEMS deflection angle. This requires dynamically adjusting the stimulation path optics to counteract the axial focal shift caused by field curvature.

We achieve this by introducing an electrically-tunable liquid lens into the stimulation optical path. The liquid lens provides a variable optical power that can be adjusted in real-time by changing the applied voltage. The adjustable optical-power range of the liquid lens is 18 D (diopters), from -5 D at an operating voltage of 34 V to 13 D at 54 V. By selecting the appropriate optical power for each MEMS deflection angle, we can compensate the Petzval sum of the stimulation path to maintain proper focus alignment.

The compensation principle is based on Petzval sum theory. The total Petzval sum of the stimulation path determines the curvature of the natural focal surface. By introducing an additional optical element (the liquid lens) with adjustable optical power, we can modify the total Petzval sum to flatten this curved focal surface, making it coincide with the planar imaging focal plane:

$$P_{total} = P_{doublets} + P_{liquid} = \sum \Phi_i / n_i + \varphi_{LL} / n_{LL} \quad (2)$$

where $P_{total}$ is the total Petzval sum of the stimulation optical path after compensation, $P_{doublets}$ is the contribution from the achromatic doublet lenses, $P_{liquid}$ is the contribution from the liquid lens, $\varphi_{LL}$ is the optical power of the liquid lens, and $n_{LL}$ is the equivalent refractive index of the liquid lens. Setting $P_{total} = 0$ ensures that the stimulation focal surface is planar and aligned with the imaging focal plane.

The key advantage of the liquid lens is its dynamic tunability. As the MEMS mirror deflects to different angles (targeting different neurons at different lateral positions), the magnitude of field curvature-induced axial shift changes. The liquid lens voltage is adjusted in real-time to provide the exact optical power needed to compensate the field curvature at each specific deflection angle:

$$\varphi_{LL}(\theta) = -n_{LL} \times \sum(\varphi_i / n_i) \quad (3)$$

where θ represents the MEMS deflection angle (X and Y components), and $\varphi_{LL}(\theta)$ is the required liquid lens optical power for that specific deflection angle.

The relationship between MEMS deflection angle and required liquid lens compensation is determined through optical simulation and can be approximated by polynomial functions. In the intended implementation, a control system would read the MEMS mirror position, calculate the required liquid lens voltage using the pre-calibrated polynomial relationship, and apply the voltage to adjust the liquid lens optical power-all within the -30 ms response time of the liquid lens (Figure 3).

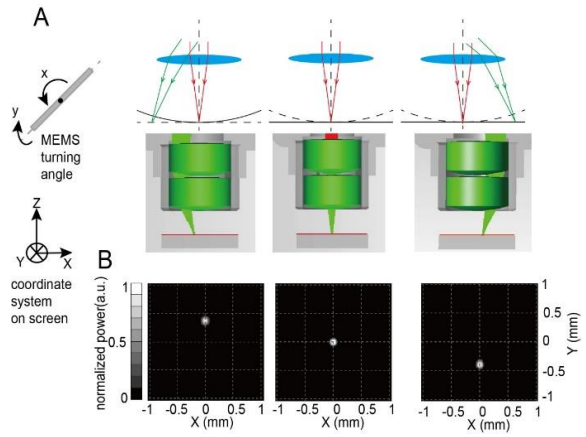


*Figure 3: Schematic diagram of liquid lens compensation for field curvature-induced focal point deviation. By placing a tunable liquid lens in the stimulation optical path before the MEMS mirror, the axial focal point displacement caused by beam deflection is corrected. Both schematic and simulation results demonstrate that the stimulation focal point returns to the imaging plane after liquid lens compensation is applied*

This dynamic compensation approach would operate adaptively based on the scanning position. When MEMS is at zero deflection (on-axis), minimal or no liquid lens compensation would be needed since the stimulation beam remains paraxial. As MEMS deflection increases for off-axis stimulation, the liquid lens optical power increases correspondingly to counteract the growing field curvature effect.

Through this coordinated adjustment, the stimulation laser focal point would remain coincident with the imaging focal plane across the entire field of view.

Importantly, the liquid lens is placed only in the stimulation path and does not affect the imaging path. The calcium imaging remains unaltered, while the stimulation path receives dynamic aberration correction.

## 3. Simulation Results

### 3.1 Simulation Model

An optical simulation model of the system was established using optical design software TracePro. The model includes all components listed in Table 1.

The simulation wavelength was set to 589 nm for the optogenetic stimulation path, corresponding to the peak absorption of ChrimsonR. The imaging wavelength range of 500-550 nm was used to evaluate the calcium imaging performance with GCaMP indicators.

### 3.2 Field Curvature Characterization

Through optical path model simulation, the stimulation laser focal point position was characterized as a function of MEMS deflection angle. The axial focal shift, measured perpendicular to the imaging focal plane and resulting from field curvature, showed a maximum displacement of 0.82 mm when MEMS deflected along the X-axis at 3.8°, and 0.22 mm when deflected along the Y-axis at the same angle. These axial shifts represent the critical mismatch between the stimulation focal point and the imaging focal plane. Without compensation, attempting to stimulate a neuron at the field edge (3.8° deflection) would result in the laser focusing up to 0.82 mm away from the intended depth-a critical error given that typical imaging depths are only 100-300 μm.

In terms of lateral targeting accuracy within the imaging focal plane, the lateral displacement range across the field of view spans ± 0.5 mm, corresponding to a MEMS scanning coverage of 500 μm × 500 μm at the sample plane. The liquid lens can be adjusted in real-time according to the MEMS deflection angle to compensate for the axial focal shift, bringing the stimulation focal point back into alignment with the imaging focal plane. For systematic characterization, MEMS mirror deflections were simulated at 0.3-degree intervals across the full scanning range up to 3.8°. This resulted in 25 deflection positions along each axis (X and Y), for a total of 625 unique positions across the two-dimensional scan range.

### 3.3 Polynomial Fitting of Field Curvature

The required liquid lens compensation curvature as a function of MEMS deflection angle was characterized through optical simulation and fitted to polynomial functions to establish empirical compensation formulas.

Some points at the extreme edges along both axes could no longer be fully corrected because of the limited tuning range of the liquid lens; therefore, these invalid edge data points were excluded. A total of 21 deflection angle positions were simulated along the X-axis, capturing the full nonlinear relationship between deflection angle and required compensation curvature. Figure 4 shows the simulation data points and polynomial fitting curves for the X-axis, Y-axis, and diagonal deflection directions. In this figure, the quantity plotted on the vertical axis represents the liquid-lens curvature required for correction, while the variable x denotes the MEMS deflection position along the corresponding axis. Specifically, for each deflection position, the off-axis focal point was corrected back onto the focal plane by tuning the liquid lens, and the corresponding curvature values were then fitted as a function of x. The analysis reveals important directional characteristics: the compensation curvature required along the Y-axis is approximately 0.1 times that of the X-axis at equivalent deflection angles, reflecting the asymmetric optical path geometry in the two scanning directions. At the maximum simulated deflection of 3.8° along the X-axis, the required compensation curvature reaches 0.34 $cm^{-1}$. For three-dimensional targeting across the full scan field, the compensation requirements were also characterized along the two diagonal deflection directions. When the MEMS deflects simultaneously in both X and Y directions at equal angles (x = y), the required compensation curvature at 3.8° combined deflection reaches 0.58 $cm^{-1}$; the orthogonal diagonal direction (x = -y) requires 0.50 $cm^{-1}$ at the same magnitude.

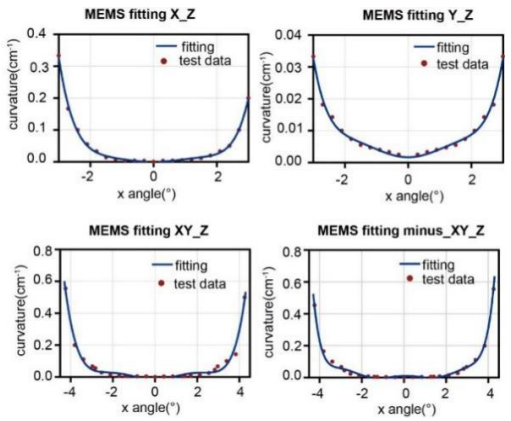


*Figure 4: Simulation results and polynomial fitting of the required liquid lens compensation curvature*

In Figure 4, the required curvature compensation along the X-rotation direction is nonlinear; at a MEMS deflection angle of 3.8°, the required compensation curvature is 0.34 $cm^{-1}$. A total of 21 simulation data points were used for curve fitting, yielding polynomial curves for interpolating the compensation curvature at arbitrary deflection angles. The required compensation curvature along the Y-direction is approximately 0.1 times that of the X-direction. For three-dimensional compensation, the required curvature was also characterized along two diagonal directions (x = y and x = −y). At a combined deflection of 3.8° in both X and Y, the required compensation curvature is 0.58 $cm^{-1}$ (x = y) and 0.50 $cm^{-1}$ (x = −y).

The fitting results on X axis is:

$$\Delta z = -0.0002773\theta_x^4 + 0.0001281\theta_x^3 + 0.01094\theta_x^2 + 0.0002313\theta_x - 0.0003579$$

The fitting results on Y axis is:

$$\Delta z = -0.0006099\theta_x^4 - 8.819e^{-19} * \theta_y^3 + 0.003054\theta_y^2 + 2.549e^{-18} * \theta_y + 0.001677$$

The fitting results on diagonal axis (x=y direction) is:

$$\Delta z = -0.003813\theta_{xy}^4 - 7.721e^{-5} * \theta_{xy}^3 + 0.0215\theta_{xy}^2 + 0.0006223\theta_{xy} - 0.01328$$

The fitting results on diagonal axis (x=-y direction) is:

$$\Delta z = 0.007261\theta_{-xy}^4 - 0.001529 * \theta_{-xy}^3 - 0.01756\theta_{-xy}^2 + 0.002851\theta_{-xy} + 0.01049$$

where Δz is the compensation curvature in $cm^{-1}$ and $\theta_x, \theta_y, \theta_{xy}, \theta_{-xy}$ respectively are the X-axis deflection angle in degrees, Y-axis deflection angle, X=Y axis deflection angle and X=-Y axis deflection angle.

The 4th-order polynomial provides superior fitting accuracy ($R^2$ = 0.9982), indicating that the field curvature relationship is highly predictable and can be accurately compensated using the empirical formula. The high $R^2$ value demonstrates that the Petzval sum theory accurately describes the field curvature behavior in this optical system.

The compensation curvature required along the Y-axis is approximately 0.1 times that of the X-axis at equivalent deflection angles, and comparable polynomial fits with high goodness-of-fit values were obtained for the Y-axis deflection. This substantial asymmetry between the X and Y axes arises from differences in the optical path geometry in the two scanning directions.

### 3.4 Compensation Performance Evaluation

To extend the one-dimensional polynomial compensation models to arbitrary two-dimensional scan positions, all simulation data were imported into MATLAB for three-dimensional surface fitting.

As shown in Figure 5, the compensation curvature across the full two-dimensional scan field was fitted using polynomial surfaces of 2nd through 5th order.

The analysis of polynomial order selection (Figure 5B and 5C) demonstrates that fitting error decreases and goodness of fit ($R^2$) improves with increasing polynomial order, with the 4th-order polynomial providing the optimal balance between model complexity and fitting accuracy. The resulting three-dimensional compensation surface constitutes the primary theoretical basis for determining the required liquid lens curvature adjustment at any arbitrary combination of MEMS X and Y deflection angles.

Compensation performance was evaluated on a 25 × 25 grid across the 1 mm × 1 mm scan range. After excluding invalid edge points, 84 valid positions along the X-axis, Y-axis, y = x direction, and y = -x direction were used; the required curvature at each point was calculated from the Figure 5 surface model.

Without liquid lens compensation, the system exhibited substantial axial targeting errors across the field of view. The mean axial error was 42.3 μm with a standard deviation of 18.7 μm, indicating considerable variability in stimulation accuracy depending on position. The maximum error reached 73.2 μm at the field corners where MEMS deflection was greatest, while the minimum error of 2.1 μm occurred near the field center where the beam remained nearly paraxial. This spatial heterogeneity in targeting accuracy would severely compromise experimental reproducibility and make it impossible to reliably stimulate neurons at different lateral positions with consistent precision.

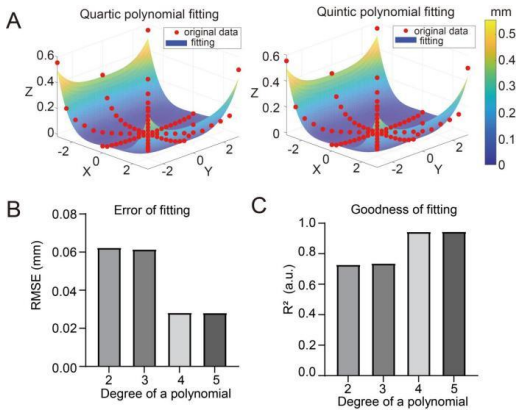


*Figure 5: Three-dimensional polynomial fitting of the compensation curvature surface. (A) All simulation data were imported into MATLAB to compute the three-dimensional fitting surface, which serves as the primary theoretical basis for determining the required liquid lens compensation at arbitrary deflection angle combinations. The data were fitted using polynomial surfaces of 2nd through 5th order. (B) Relationship between polynomial order and fitting error. (C) Relationship between polynomial order and goodness of fit ($R^2$)*

With liquid lens compensation, the targeting accuracy improved dramatically. The mean axial error decreased to 5.8 μm with a standard deviation of only 2.4 μm, demonstrating not only better average performance but also much more uniform accuracy across the field. The maximum error was reduced to 12.1 μm and the minimum error was 1.8 μm, indicating that the compensation effectively flattened the field curvature and maintained consistent focus alignment throughout the scanning range. The compensation method thus achieves approximately 7-fold improvement in mean axial positioning accuracy (42.3 μm → 5.8 μm), with the standard deviation decreasing significantly (18.7 μm → 2.4 μm) to provide consistent performance across the entire field of view.

The residual axial error of 5.8 μm after compensation can be attributed to several factors. First, the discrete voltage control steps of the liquid lens impose finite voltage resolution, preventing perfect compensation at all field positions. Second, higher-order aberrations not accounted for in the Petzval sum calculation, such as spherical aberration and coma, become more significant at larger field angles and contribute to residual errors. Third, manufacturing tolerances in the optical components, particularly in the achromatic doublets and MEMS mirror flatness, introduce small deviations from the ideal optical design. Fourth, numerical precision limitations in the simulation itself may contribute to the measured residual error. Nevertheless, the achieved positioning accuracy of 5.8 μm axial and 6.2 μm lateral is well within the requirements for single-cell optogenetic stimulation, as typical neuronal soma diameters range from 10-20 μm.

## 4. Discussion

The optical simulation results systematically validate the proposed compensation design. Without compensation, axial focal point shift averages 42.3 μm with maximum shifts exceeding 73 μm at field corners-displacements that far exceed neuronal soma diameters and would cause significant targeting errors in physical implementations. The field curvature exhibits a predictable relationship with deflection angle, accurately modeled using polynomial functions with $R^2 = 0.9982$, confirming that this systematic aberration is amenable to correction via adaptive optics. The liquid lens compensation design achieves 7-fold improvement in mean axial error (42.3 μm to 5.8 μm) with reduced standard deviation (18.7 μm to 2.4 μm), enabling reliable single-cell targeting precision. The 30 ms liquid lens response time supports dynamic closed-loop control at frequencies up to 30 Hz, adequate for tracking calcium transients (50-200 ms dynamics).

The proposed design offers several advantages validated through simulation. Integration of MEMS scanning mirrors and liquid lenses enables compact architecture implementable in lightweight (<5 grams) packages suitable for head-mounted applications, achieving cellular-level positioning precision (5.8 μm axial, 6.2 μm lateral) comparable to bench-top systems. Component costs are substantially lower than spatial light modulators or deformable mirrors, offering practical balance between functionality, size, and cost. From an optical engineering perspective, this work provides quantitative characterization of field curvature in MEMS-based dual-path systems, demonstrates that dynamic Petzval sum compensation can be achieved with simple polynomial control laws ($R^2 = 0.9982$), and establishes a validated design framework using commercially available components adaptable to other miniaturized scanning applications including endoscopy and mobile imaging systems.

Several limitations should be acknowledged. The field of view is limited to 500 μm × 500 μm, the design performs sequential rather than simultaneous multi-site stimulation, and single-photon imaging restricts penetration depth to <300 μm. Most importantly, this work is based on optical simulation using TracePro. While rigorous modeling with realistic component specifications and strong theoretical foundation ($R^2 = 0.9982$) provide important design validation, experimental verification with physical prototypes is necessary to characterize real-world performance including alignment sensitivity, vibration effects, thermal drift, and manufacturing tolerances. Nevertheless, the simulation-based study provides crucial theoretical foundation and quantitative predictions to guide future physical implementation. Future refinements could include two-photon microscopy integration for deeper tissue access and faster liquid lens designs for higher-frequency control.

Compared to existing technologies, the MEMS-liquid lens design fills a specific niche. Optical fiber stimulation lacks cellular-level precision, while DMD and SLM-based holographic approaches are too large and power-intensive for head-mounted applications. The proposed approach achieves favorable balance among miniaturization, precision, and cost, making it well-suited for freely behaving animal applications requiring single-cell resolution. Recent miniaturized optogenetic systems have not specifically addressed field curvature correction, suggesting this liquid lens compensation method could potentially be integrated with existing platforms to improve axial positioning accuracy.

## 5. Conclusions

This study presents a systematic design and simulation of field curvature compensation in MEMS-based miniaturized microscopes for optogenetic applications. Through Petzval sum theory analysis and rigorous TracePro simulation, we characterized how MEMS deflection causes axial focal shift and developed an innovative compensation method using electrically-controlled liquid lenses for real-time aberration correction. The simulation demonstrates 7-fold improvement in axial positioning accuracy (42.3 μm to 5.8 μm), achieving precision sufficient for single-cell targeting. The high goodness-of-fit ($R^2 = 0.9982$) validates the design methodology, and the 30 ms response time enables dynamic control at frequencies up to 30 Hz, adequate for neural activity manipulation. The compact, lightweight design is suitable for future head-mounted implementations in freely behaving animals.

This work provides important contributions to miniaturized optical systems. It offers systematic quantitative characterization of field curvature in MEMS-based dual-path imaging/stimulation geometries, demonstrates that dynamic Petzval sum compensation using tunable liquid lenses is viable with predictable performance, and establishes a validated design methodology using commercially available components. The simulation-based approach provides theoretical foundation and practical guidance for developing next-generation miniaturized optical systems requiring precise three-dimensional beam positioning, with potential applications extending to endoscopy, mobile imaging systems, and other compact scanning devices.

Future work will focus on experimental validation through physical prototype construction to characterize real-world performance including alignment sensitivity and thermal stability, extension

to two-photon imaging for deeper tissue access, and development of closed-loop control algorithms for activity-dependent optogenetic stimulation.

## Acknowledgement

This research was funded by 2024 Yinchuan Science and Technology Plan Project (2024GXHZC004).

## References

[1] Helmchen, F., & Denk, W. (2005). Deep tissue two-photon microscopy. *Nature Methods*, 2(12), 932–940. https://doi.org/10.1038/nmeth818

[2] Grienberger, C., & Konnerth, A. (2012). Imaging calcium in neurons. *Neuron*, 73(5), 862–885. https://doi.org/10.1016/j.neuron.2012.02.011

[3] Deisseroth, K. (2015). Optogenetics: 10 years of microbial opsins in neuroscience. *Nature Neuroscience*, 18(9), 1213–1225. https://doi.org/10.1038/nn.4091

[4] Boyden, E.S., Zhang, F., Bamberg, E., Nagel, G., & Deisseroth, K. (2005). Millisecond-timescale, genetically targeted optical control of neural activity. *Nature Neuroscience*, 8(9), 1263–1268. https://doi.org/10.1038/nn1525

[5] Chen, T.W., Wardill, T.J., Sun, Y., Pulver, S.R., Renninger, S.L., Baohan, A., Schreiter, E.R., Kerr, R.A., Orger, M.B., Jayaraman, V., Looger, L.L., Karel Svoboda, K., & Douglas S. Kim, D.S. (2013). Ultrasensitive fluorescent proteins for imaging neuronal activity. *Nature*, 499(7458), 295–300. https://doi.org/10.1038/nature12354

[6] Dana, H., Sun, Y., Mohar, B., Hulse, B.K., Kerlin, A.M., Hasseman, J.P., Tsegaye, G., Tsang, A., Wong, A., Patel, R., John J. Macklin, J.J., Yang Chen, Y., Arthur Konnerth, A., Jayaraman, V., Loren L. Looger, L.L., Schreiter, E,R, Svoboda, K., & Douglas S. Kim, D.S. (2019). High-performance calcium sensors for imaging activity in neuronal populations and microcompartments. *Nature Methods*, 16(7), 649–657. https://doi.org/10.1038/s41592-019-0435-6

[7] Cai, D.J., Aharoni, D., Shuman, T., Shobe, J., Biane, J., Song, W., Wei, B., Veshkini, M., La-Vu, M., Lou, J., Flores, S.E., Kim, I., Sano, Y., Zhou, M., Baumgaertel, K., Lavi, A., Kamata, M., Tuszynski, M., Mayford, M., Golshani, P., & Silva, A.J. (2016). A shared neural ensemble links distinct contextual memories encoded close in time. Nature, 534(7605), 115–118. https://doi.org/10.1038/nature17955

[8] Zong, W., Wu, R., Li, M., Hu, Y., Li, Y., Li, J., Rong, H., Wu, H., Xu, Y., Lu, Y., Jia, H., Fan, M., Zhou, Z., Zhang, Y., Wang, A., Chen, L., & Cheng, H. (2017). Fast high-resolution miniature two-photon microscopy for brain imaging in freely behaving mice. Nature Methods, 14(7), 713–719. https://doi.org/10.1038/nmeth.4305

[9] Skocek, O., Nöbauer, T., Weilguny, L., Traub, F.M., Xia, C.N., Molodtsov, M.I., Grama, A., Yamagata, M., Aharoni, D., Cox, D.C., Golshani, P., & Vaziri, A. (2018). High-speed volumetric imaging of neuronal activity in freely moving rodents. *Nature Methods*, 15(6), 429–432. https://doi.org/10.1038/s41592-018-0008-0

[10] Zhang, L., Liang, B., Barbera, G., Hawes, S., Zhang, Y., Stump, K., Baum, I., Yang, Y., Li, Y., & Lin, D.-T. (2019). Miniscope GRIN lens system for calcium imaging of neuronal activity from deep brain structures in behaving animals. *Current Protocols in Neuroscience*, 86(1), e56. https://doi.org/10.1002/cpns.56

[11] Stamatakis, A.M., Schachter, M.J., Gulati, S., Zitelli, K.T., Malanowski, S., Tajik, A., Fritz, C., Trulson, M., & Otte, S.L. (2018). Simultaneous optogenetics and cellular resolution calcium imaging during active behavior using a miniaturized microscope. Frontiers in Neuroscience, 12, 496. https://doi.org/10.3389/fnins.2018.00496

[12] Futia, G.L., Zohrabi, M., McCullough, C., Teel, A., de Souza, F.S., Oroke, R., Bright, V.M., Restrepo, D., Gopinath, J.T., & Gibson, E.A. (2024). Opto2P-FCM: A MEMS based miniature two-photon microscope with two-photon patterned optogenetic stimulation. *In: Optica Biophotonics Congress: Biomedical Optics 2024 (Translational, Microscopy, OCT, OTS, BRAIN), Technical Digest Series (Optica Publishing Group, 2024), paper JS4A.56*. https://doi.org/10.1364/translational.2024.js4a.56

[13] Holmstrom, S.T., Baran, U., & Urey, H. (2014). MEMS laser scanners: a review. *Journal of Microelectromechanical Systems*, 23(2), 259–275. https://doi.org/10.1109/JMEMS.2013.2295470

[14] Yalcinkaya, A.D., Urey, H., Brown, D., Montague, T., & Sprague, R. (2006). Two-axis electromagnetic microscanner for high resolution displays. *Journal of Microelectromechanical Systems*, 15(4), 786–794. https://doi.org/10.1109/JMEMS.2006.879380

[15] Wu, L., Xie, H., Gong, Y., Zhang, Y., Chen, Z., & Xie, H. (2017). MEMS-based varifocal micromirror for 3D shape measurement. *Sensors*, 17(7), 1527. https://doi.org/10.3390/s17071527

[16] Li, L., Wu, L., Gong, Y., Xie, H., & Shi, Y. (2022). Varifocal MEMS mirrors for high-speed axial focus scanning: a review. *Microsystems & Nanoengineering*, 8(1), 137. https://doi.org/10.1038/s41378-022-00481-0

[17] Papagiakoumou, E., Anselmi, F., Bègue, A., de Sars, V., Glückstad, J., Isacoff, E.Y., & Emiliani, V. (2010). Scanless two-photon excitation of channelrhodopsin-2. *Nature Methods*, 7(10), 848–854. https://doi.org/10.1038/nmeth.1505

[18] Packer, A.M., Russell, L.E., Dalgleish, H.W., & Häusser, M. (2015). Simultaneous all-optical manipulation and recording of neural circuit activity with cellular resolution in vivo. *Nature Methods*, 12(2), 140–146. https://doi.org/10.1038/nmeth.3217

[19] Smith, W.J. (2007). *Modern optical engineering: The design of optical systems* (4th ed.). McGraw-Hill.

[20] Gross, H., Zügge, H., Peschka, M., & Blechinger, F. (2005). *Handbook of optical systems, volume 3: Aberration theory and correction of optical systems*. Wiley-VCH.

[21] Sasian, J. (2013). *Introduction to aberrations in optical imaging systems*. Cambridge University Press. https://doi.org/10.1017/CBO9780511795183.001

[22] Mahajan, V.N. (2014). *Optical imaging and aberrations, part II: Wave diffraction optics* (2nd ed.). SPIE Press. https://doi.org/10.1117/3.898443

[23] Berge, B., & Peseux, J. (2000). Variable focal lens controlled by an external voltage: An application of electrowetting. *European Physical Journal E*, 3(2), 159–163. https://doi.org/10.1007/s101890070029

[24] Kuiper, S., & Hendriks, B.H. (2004). Variable-focus liquid lens for miniature cameras. *Applied Physics Letters*, 85(7), 1128–1130. https://doi.org/10.1063/1.1779954

[25] Zhang, D.Y., Lien, V., Berdichevsky, Y., Choi, J., & Lo, Y.H. (2003). Fluidic adaptive lens with high focal length tunability. *Applied Physics Letters*, 82(19), 3171–3173. https://doi.org/10.1063/1.1573337

[26] Mermillod-Blondin, A., McLeod, E., & Arnold, C.B. (2008). High-speed varifocal imaging with a tunable acoustic gradient index of refraction lens. *Optics Letters*, 33(18), 2146–2148. https://doi.org/10.1364/OL.33.002146

[27] Fuh, Y.-K., Chen, J.-K., & Chen, P.-W. (2015). Characterization of electrically tunable liquid lens and adaptive optics for aberration correction. *Optics Express*, 23(20), 26119–26131. https://doi.org/10.1016/j.ijleo.2015.09.105

[28] Waibel, P., Meinert, T., Uhl, R., Czarske, J., & Isenberg, B. (2019). Optical performance evaluation and chromatic aberration correction of a focus tunable lens used for 3D microscopy. *Biomedical Optics Express*, 10(12), 6029–6044. https://doi.org/10.1364/BOE.10.006029

[29] Ren, H., Fox, D., Anderson, P.A., Wu, B., & Wu, S. T. (2006). Tunable-focus liquid lens controlled using a servo motor. *Optics Express*, 14(18), 8031–8036. https://doi.org/10.1364/OE.14.008031

[30] Wang, L., Oku, H., & Ishikawa, M. (2015). Variable-focus lens with 30 mm optical aperture based on liquid-membrane-liquid structure. *Applied Physics Letters*, 102(13), 131111. https://doi.org/10.1063/1.4800603